An approach to reduce light field sampling redundancy for flame temperature reconstruction

QI QI,[1] MD. MOINUL HOSSAIN,[2] JIN-JIAN LI,[1] BIAO ZHANG, [1,*] JIAN LI[1] AND CHUAN-LONG XU[1,*]

[1] *National Engineering Research Center of Turbo-Generator Vibration, School of Energy and Environment, Southeast University, Nanjing 210096, China*

[2] *School of Engineering and Digital Arts, University of Kent, Canterbury, Kent, CT2 7NT, UK*

[*] *chuanlongxu@seu.edu.cn* (*Chuan-long Xu*), *zhangbiao@seu.edu.cn* (*Biao Zhang*)

Abstract: Flame temperature measurement through a light field camera shows an attractive research interest due to its capabilities of obtaining spatial and angular rays' information by a single exposure. However, the sampling information collected by the light field camera is vast and most of them are redundant. The reconstruction process occupies a larger computing memory and time-consuming. We propose a novel approach i.e., feature rays under-sampling (FRUS) to reduce the light field sampling redundancy and thus improve the reconstruction efficiency. The proposed approach is evaluated through numerical and experimental studies. Effects of under-sampling methods, flame dividing voxels, noise levels and light field camera parameters are investigated. It has been observed that the proposed approach provides better anti-noise ability and reconstruction efficiency. It can be valuable not only for the flame temperature reconstruction but also for other applications such as particle image velocimetry and light field microscope.

1. Introduction

Radiative imaging techniques have become attractive tools in the field of combustion diagnostics [1-3]. Various parameters of flame such as temperature, species concentration, velocity and pressure can be measured through these techniques. Compared with the intrusive techniques such as thermocouples [4] and laser-based imaging techniques (i.e., Tunable Diode Laser Absorption Spectroscopy [5], Planar Laser-induced Fluorescence [6], and Laser-Induced Incandescence [7]), the radiative imaging techniques are non-intrusive, easy to setup and cost-effective. These techniques have also been recognized as effective and accurate techniques for flame temperature measurement. Various radiative imaging techniques have been developed based on conventional Charge Coupled Device (CCD)/Complementary Metal Oxide Semiconductor (CMOS) camera [8], optic imaging fibers [9] and light field cameras [10-12]

for combustion diagnostics. The conventional CCD camera captures a 2D flame image from a certain perspective which is considered as a projection. Typically, multiple cameras are required to collect flame images from different perspectives to reconstruct flame parameters accurately. However, the number of cameras lead to a complicated system setup and demands an appropriate synchronization mechanism [13]. Optical imaging fibers based system offers excellent flexibility and transferability of the system [14]. However, still requires a proper synchronization mechanism and provides lower resolution images.

A light field camera equips a microlens array (MLA) between the main lens and photosensor, and therefore both spatial and angular information can be achieved by a single exposure [15]. This technique overcomes the limitations of multi-camera based radiative imaging techniques. In recent years, light field camera-based techniques have been used for flame temperature measurement. For example, Sun *et al*. used a single light field camera to reconstruct 3D flame temperature distribution [16]. Kelly *et al*. studied a multi-band plenoptic pyrometer to reconstruct flame temperature in a solid rocket strand burner plume [17]. Zhao *et al*. reconstructed candle flame temperature through a combination of optical sectioning tomography and light field camera techniques [18]. Multi-light field camera systems are also developed to reconstruct complex flame temperature distribution. For instance, Qi *et al*. proposed a multi-plenoptic camera system to collect flame images from different perspectives to retrieve the flame temperature field [19]. The aforementioned works represent the state-of-the-art of light field imaging for flame temperature diagnostics.

Despite these various developments, the light field camera is not flawless. Because the microlens separates detection rays on the imaging plane of the main lens in the light field camera, the limitation of this camera structure is that the ray's angle separated by a microlens varies a little. For instance, a microlens covers about 200 pixels, however, the angles of rays detected by pixels under a microlens only differ from 21.5° to 23.5°, thus there is little difference between adjacent rays [20]. These rays provide similar sampling information. As a result, most of the radiative information recorded by the light field camera is redundant and thus creates an overdetermined problem for the flame temperature reconstruction. Meanwhile, the number of the voxel that each ray crosses through is far less than the total number of voxels, so the reconstruction is also an ill-condition and ill-posed problem. Therefore, the reconstruction process requires large computing resources for large matrix storage and time-consuming, especially the reconstruction of a high-resolution temperature field or simultaneous reconstruction of multiple flame radiative properties [21].

To address the problems, various studies have been conducted to improve the light field sampling quality. For instance, Wei *et al*. introduced sample irregularities and lens aberrations into light field camera design to improve the quality and usability of light field cameras [22]. Schedl *et al*. used a compressed sensing reconstruction technique to upsample a sparse light field to a dense light field to improve the resolution of the light fields [23]. Park *et al*. presented

an electrically fast-switching virtual-moving array to enhance the light field spatial resolution [24]. Huang *et al*. proposed a systematic approach to model and analyze the ray position sampling issue and characterized the effects of ray position sampling on the visual response [25]. Zhu *et al*. presented a spectral analysis for sampling the light field signal using a Fourier transform [26] . Although these methods improve the light field sampling quality, the problem of light field ray's redundancy is not investigated. Sampling characteristics of the light field cameras for flame temperature measurement has also been investigated. For instance, Liu *et al*. reported that the sampling characteristics depend on light field camera parameters such as focal length and magnification of both the main lens and microlens [27]. Sun *et al*. studied the sampling characteristics among different light field cameras such as traditional and focused light field cameras [28]. The sampling characteristics and the effects of camera parameters on sampling properties were not studied to reduce the light field sampling redundancy. Therefore, it is crucial to investigate an approach to reduce the light field sampling redundancy for flame temperature reconstruction.

In this study, a novel feature rays under-sampling approach is proposed to reduce the light field sampling redundancy and thus improve the reconstruction efficiency. According to the ray's distribution and angle characteristics, the proposed approach performs ray and azimuthal angle clustering to obtain representative feature rays. The flame temperature is then reconstructed using these feature rays. The proposed approach is systematically evaluated through numerical studies under different under-sampling methods, flame dividing voxels, noise levels and light field camera parameters. Experimental studies were also conducted to reconstruct the ethylene diffusion flames temperature to verify the applicability of the approach. The results obtained from numerical and experimental studies are presented and discussed.

2. Methodology

2.1 Light field imaging model

The light field camera captures the spatial and angular information of the ray by a single exposure. This information is known as light field sampling [29, 30]. The light field camera mainly consists of a main lens, MLA and a photosensor. The parameters of the light field camera are shown in Table 1. Fig. 1 shows the principal architecture of the light field imaging model. The imaging model is divided into two parts such as (1) imaging by the main lens and (2) imaging by the MLA. Since the cone angle of a ray detected by the pixel is so small (i.e., <0.015°), the ray which passes through the pixel and the center of its corresponding microlens is used to represent the beam. This ray is called the corresponding ray of the pixel [16]. It must be traced from the photosensor pixel to the flame to obtain the spatial and angular information.

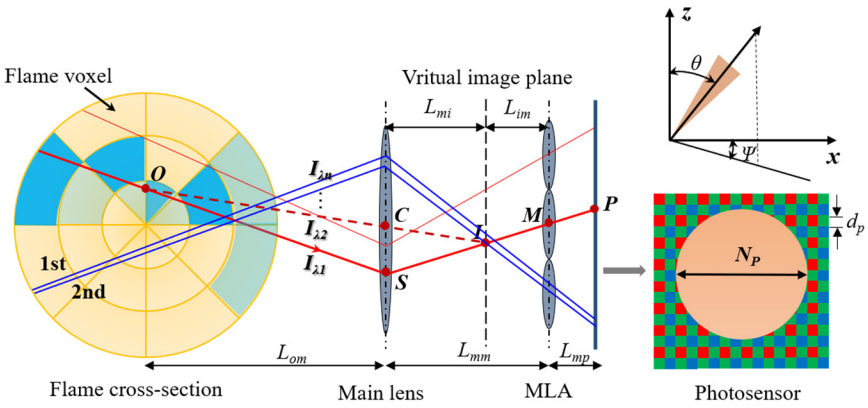

Fig. 1. The principal architecture of the light field imaging model.

Table 1. The parameters of the light field camera.

Symbol	Unit	Description
f	mm	the focal length of the main
f_m	mm	the focal length of the microlens
d_p	mm	length of the pixel
L_{mm}	mm	the distance between the main lens and MLA
L_{mp}	mm	the distance between the MLA and photosensor
L_{om}	mm	the distance between the flame centerline and main lens
L_{im}	mm	the distance between the virtual image plane and MLA
L_{mi}	mm	the distance between the main lens and virtual image plane
N_m		number of microlenses
N_p		number of pixels covered by each microlens

The light field camera can be divided into traditional and focused light field cameras based on the distance between the photosensor and the MLA [28]. For the focused light field camera, the L_{mm} is not equal to the f_m of the microlens, (i.e., $L_{mm} \neq f_m$). The flame centerline is in the object plane of the light field camera to ensure that the light field camera focuses the flame accurately. Therefore, the object plane is the conjugate plane of the virtual image plane for the main lens, and the photosensor is the conjugate plane of the virtual image plane for the MLA. For the traditional light field camera i.e., $L_{mm} = f_m$, the object plane and MLA are conjugated to the main lens. At this time, the virtual image plane is the plane where the MLA is located. Therefore, the spatial and angular information of rays can be achieved by the following Eqs. (1-6).

$$\frac{1}{L_{im}}+\frac{1}{L_{mp}}=\frac{1}{f_m} \tag{1}$$

$$\frac{y_P-y_M}{y_I-y_M}=\frac{z_P-z_M}{z_I-z_M}=-\frac{L_{mp}}{L_{im}} \tag{2}$$

$$\frac{1}{L_{om}}+\frac{1}{L_{mi}}=\frac{1}{f} \tag{3}$$

$$\frac{y_M-y_C}{y_O-y_C}=\frac{z_M-z_C}{z_O-z_C}=-\frac{L_{mi}}{L_{om}} \tag{4}$$

$$\theta=\arccos\left[\frac{\left(z_S-z_O\right)}{\sqrt{{L_{om}}^2+\left(y_S-y_O\right)^2+\left(z_S-z_O\right)^2}}\right] \tag{5}$$

$$\psi=\begin{cases}\arctan\left(\dfrac{y_S-y_O}{x_S-x_O}\right), y_S\geq y_O, x_S\neq x_O\\ \arctan\left(\dfrac{y_S-y_O}{x_S-x_O}\right)+2\pi, y_S<y_O, x_S\neq x_O\end{cases} \tag{6}$$

where (x_P, y_P, z_P) is the coordinate of point P on the photosensor; (x_M, y_M, z_M) is the coordinate of point M; (x_C, y_C, z_C) is the central coordinate of the main lens; (x_S, y_S, z_S) is the coordinate of the S; (x_O, y_O, z_O) is the coordinate at which the ray intersects the center line of the flame; θ and Ψ are the polar and azimuthal angles of the ray's direction, respectively.

2.2 Feature rays under-sampling approach

The light field camera collects a huge number of rays and these rays are separated by the MLA. The angle difference between these rays is so small and thus most of these rays are redundant and provide similar light field information. Without reducing the redundancy information, the flame reconstruction process requires a larger computing memory space for matrix storage also time-consuming. Therefore, it is crucial to reduce redundant sampling information and optimize light field sampling. In practice, the dimension of flame height is much larger than the radial dimension [31, 32]. So, the variation of ray in the polar angle is much greater than the azimuthal angle. In this study, we proposed a feature rays under-sampling (FRUS) approach to reduce the light field sampling redundancy. This approach is based on the characteristics of the ray's angle and the Douglas–Peucker (DP) algorithm. The DP algorithm is a common curve vector data

resampling technique that is often used to simplify the vector features in geographic systems [33]. It requires at least three points to represent a line.

Fig. 2 shows an example of optimized light field sampling which is achieved by the proposed approach. In this example, the flame is divided into $N_z \times N_r \times N_\varphi = 6 \times 8 \times 10$ voxels and the light field camera parameters used are listed in Table 2. A total of 518400 pixels on the photosensor can be seen in Fig. 2(a) where one pixel corresponds to one ray as described in Section 2.1 and thus in total 518400 rays are traced from the photosensor to flame. Fig. 2(a) demonstrates the effective rays (i.e., the rays that pass through a flame) and their corresponding pixels [highlighted as red box]. The rest of the rays are invalid and their corresponding pixels are black. There are in total 28867 effective rays pass through the flame voxels and their corresponding pixels are marked as the same color (refer to 1st and 2nd rays in Fig. 1). For example, in Fig. 2(b) the pixels marked as green, their corresponding rays pass through the same flame voxels. A vast number of rays are traced and most of them pass through the same flame voxels and most of them are redundant. The final feature rays and their corresponding pixels of 5070 are achieved by the proposed approach as shown in Fig. 2(c). The redundant rays are significantly reduced and thus optimized the light field sampling. Fig. 3 shows the implementation procedures of the FRUS approach.

Table 2. Key parameter values of the light field camera.

L_{om}	L_{mm}	$L_{mp}(\times f_m)$	L_{mi}	L_{im}	f	f_m	N_m	N_p	d_p
505	53.1	0.8	55.5	-2.4	50	0.6	60	12	0.008

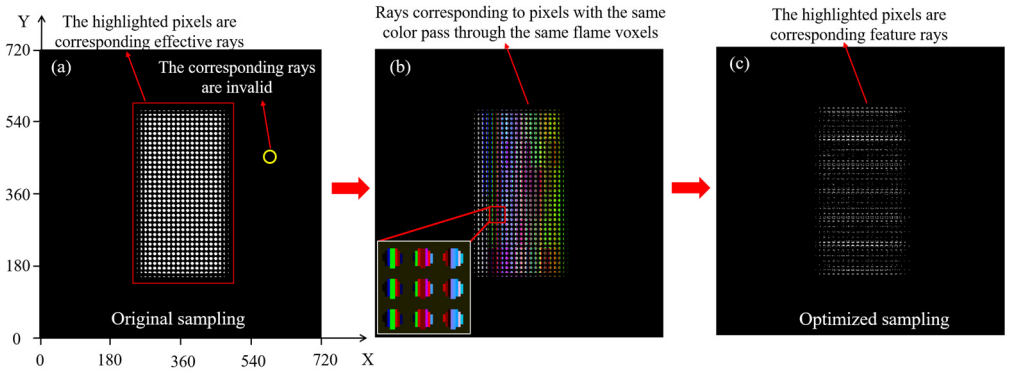

Fig. 2. A process of optimizing light field sampling through the proposed FRUS approach.

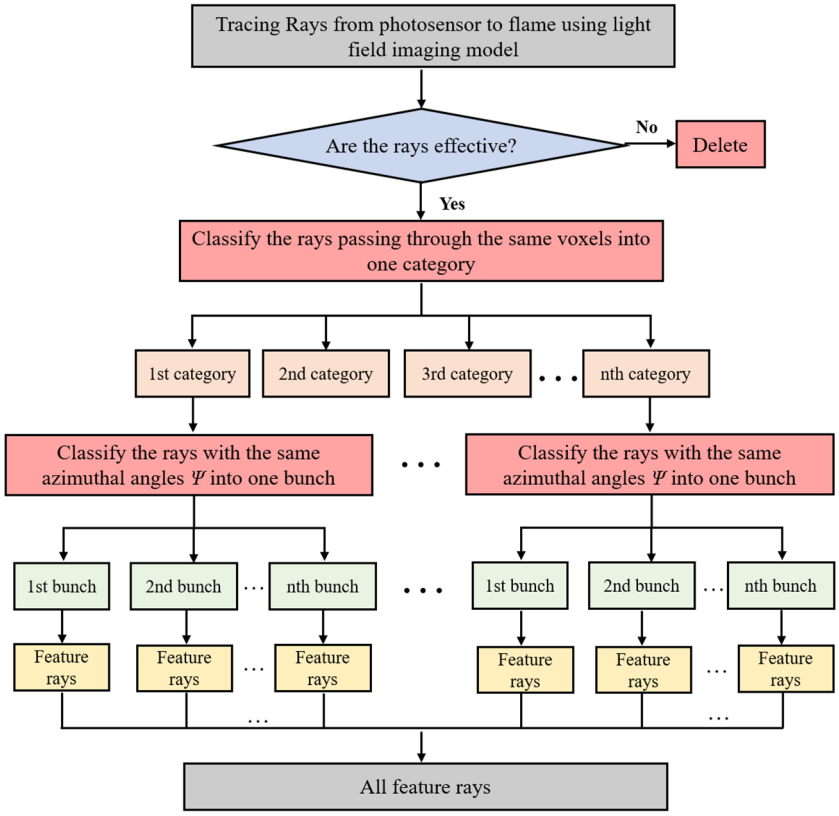

Fig. 3. Implementation approach of the proposed FRUS method.

The detailed procedures of the FRUS approach are described in **Steps** 1-6.

Step 1. Ray tracing: According to the light field imaging model, as proposed in Section 2.1, the ray corresponding to each pixel traces from the photosensor to flame.

Step 2. Identify effective ray: If the ray passing through the flame, define this ray as an effective ray and then record the angle θ, Ψ, and the voxel number of the effective, then go to Step 3. Otherwise, it is an invalid ray and deletes it.

Step 3. Ray clustering: Classify the effective rays into one category that are passing through the same flame voxels.

Step 4. Azimuthal angle Ψ clustering: The azimuthal angle Ψ clustering is carried out based on the distribution of the azimuthal angles Ψ. Classify the rays with the same azimuthal angles Ψ into one bunch and obtain the distribution of polar angle θ of each bunch.

Step 5. Feature ray's selection: Firstly, three feature polar angles θ i.e., maximum, minimum, and closest value to the average of each bunch can be selected. Secondly, feature rays corresponding to these feature polar angles can be obtained.

Step 6. Obtain all feature rays: Go through all the bunches using Step 5 and acquire the final feature rays.

2.3 Flame radiative transfer model

The optimize spatial, angular and intensity information of light field flame images can be obtained through the proposed FRUS approach, as discussed in Section 2.2 [31]. The outgoing radiative intensity at the boundary surface of a flame is the accumulation of radiative intensity of all object points along the propagation path. The radiative transfer process within the flame can be described by the Radiative Transfer Eq. (RTE) [34]:

$$\frac{\mathrm{d}I_\lambda(r,\mathbf{\Omega})}{\mathrm{d}r}=-\beta_\lambda(r)I_\lambda(r,\mathbf{\Omega})+\kappa_{\mathrm{a}\lambda}(r)I_{\mathrm{b}\lambda}(r)+\frac{\sigma_{\mathrm{s}\lambda}(r)}{4\pi}\int_{4\pi}I_\lambda(r,\mathbf{\Omega}')\Phi(\mathbf{\Omega}',\mathbf{\Omega})\mathrm{d}\mathbf{\Omega}' \tag{7}$$

where $I_\lambda(r, \mathbf{\Omega})$ represents the spectral radiative intensity at position r and direction $\mathbf{\Omega}$, [W/(m^2·μm·sr)]; $I_{\mathrm{b}\lambda}(r)$ is the spectral blackbody radiative intensity at position r, [W/(m^2·μm·sr)]; $\beta_\lambda(r)$, $\kappa_{\mathrm{a}\lambda}(r)$, $\sigma_{\mathrm{s}\lambda}(r)$ are the extinction, absorption and scattering coefficient, respectively, [m^{-1}]; $\Phi(\mathbf{\Omega}', \mathbf{\Omega})$ represents the scattering phase function of the incident in $\mathbf{\Omega}'$ direction and scattering in the $\mathbf{\Omega}$ direction.

In this study, the ambient radiation is ignored because the flame temperature is higher than the environmental temperature. Since the soot particles are absorptive, the scattering contribution of the soot particles within flame is neglected [35]. If the propagation path is divided into n parts and each path is kept at a nearly uniformed temperature, the radiative intensity at the boundary of flame in $\mathbf{\Omega}$ direction can be obtained through the discretized solution as follows:

$$I_\lambda(\mathbf{\Omega})=I_{b\lambda}^n\left[1-\exp(-\tau_{\lambda n})\right]+\sum_{i=1}^{n-1}\left[\exp\left(-\sum_{j=i+1}^{n}\tau_{\lambda j}\right)-\exp\left(-\sum_{j=i}^{n}\tau_{\lambda j}\right)\right]I_{b\lambda}^i \tag{8}$$

where τ_λ is the optical thickness of the voxel. The outgoing radiative intensity distribution at the boundary of flame can be obtained by integrating the radiative transfer process along with different directions. It can be expressed in a matrix format and described as follows:

$$\begin{bmatrix} I_\lambda^1 \\ I_\lambda^2 \\ \vdots \\ I_\lambda^M \end{bmatrix}=\begin{bmatrix} A_1^1 & A_2^1 & \cdots & A_N^1 \\ A_1^2 & A_2^2 & \cdots & A_N^2 \\ \vdots & \vdots & \ddots & \vdots \\ A_1^M & A_2^M & \cdots & A_N^M \end{bmatrix}\begin{bmatrix} I_{b\lambda}^1 \\ I_{b\lambda}^2 \\ \vdots \\ I_{b\lambda}^N \end{bmatrix} \tag{9}$$

where M and N are the total numbers of detection rays and voxels.

It is necessary to solve Eq. (9) for obtaining $I_{\mathrm{b}\lambda}$ in each voxel. Then, the temperature T in each voxel can be solved by Planck's law [36].

3. Numerical simulation

3.1 Simulation setup

To investigate the performance of the proposed FRUS approach, numerical simulations were carried out. The simulations were performed on a server with Intel(R) Core (TM) i9-9900K CPU @ 3.60GHz. In this study, a cylindrical simulated flame is considered in the simulation. The radius (R) and axial length (Z) of the simulated flame are set to 0.0066 m and 0.025 m, respectively. The simulated flame is divided into circumferential (N_z)×radial (N_r)×axial (N_φ) voxels. Fig. 4 illustrates the example of flame division voxels. The temperature distribution of two different flame structures named unimodal and bimodal is generated through Eqs. (10) and (11). Their temperature distributions are shown in Fig. 5. A Non-Negative Least Squares (NNLS) algorithm [37] is used to reconstruct the flame temperature. The absorption coefficient of ethylene flame is set to 10 m^{-1} [38].

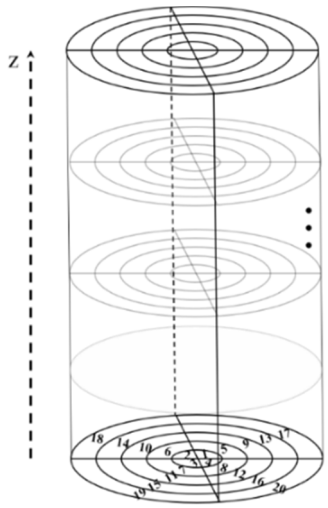

Fig. 4. Example of flame divisions voxels.

$$T(r,z)=1200\exp\left\{-\left[3\left(\frac{r^2}{R^2}+\frac{z^2}{Z^2}\right)-0.9\right]^2\right\}+900\ [\mathrm{K}] \tag{10}$$

$$T(x,y,z)=\frac{2200}{3}\left\{\begin{array}{l}\exp\left\{\begin{array}{l}-40\left[(750x+7.5)/9-1.1\right]^2\\-25\left[(750y+8.5)/9-0.8\right]^2\end{array}\right\}+\\0.8\exp\left\{\begin{array}{l}-25\left[(750x+7.5)/9-0.8\right]^2\\-35\left[(750y+8.5)/9-1.2\right]^2\end{array}\right\}\end{array}\right\}+880(1-100z/3)+753\ [\mathrm{K}] \tag{11}$$

where x, y, z and r are the coordinates of the cylindrical flame, respectively.

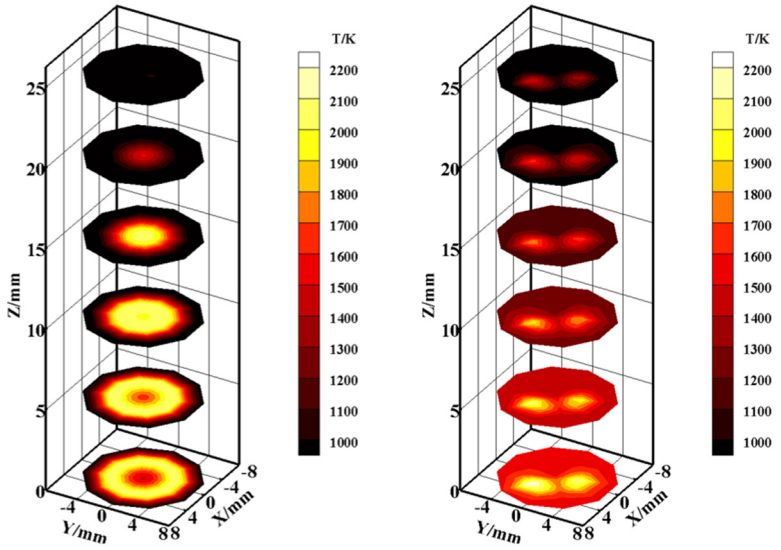

Fig. 5. The simulated flame temperature distributions.

The impacts of under-sampling methods, noise levels, flame dividing voxels and light field camera parameters on the temperature reconstruction are investigated. To evaluate the reconstruction performance, relative errors of the reconstructed temperature ΔT at ith voxel and mean relative error ΔT_{mean} are calculated by Eqs. (12) and (13).

$$\Delta T_i = \frac{\left| T_{rst,i} - T_{ori,i} \right|}{T_{ori,i}} \tag{12}$$

$$\Delta T_{\text{mean}} = \frac{1}{N} \sum_{i=1}^{n} \Delta T_i \tag{13}$$

where $T_{rst,i}$ is the reconstructed temperature at ith voxel, $T_{ori,i}$ is the original temperature at ith voxel, N is the total number of voxels.

3.2 Anti-noise ability of the FRUS approach

To examine the anti-noise ability of the FRUS approach, various noises (γ) were added to both original and FURS optimized sampling of bimodal flame radiative intensity (refer to Eq. 11) through the Eqs. (14 -16):

$$I_{mea} = (1 + \sigma\zeta) I_{exa} \tag{14}$$

where I_{mea} is the measured outgoing radiative intensity at exiting boundaries of flame, ζ is a

standard normal distribution random variable. The standard deviations of measured transmittance and reflectance σ for a γ at 99% confidence are determined as:

$$\sigma = \frac{I_{exa} \times \gamma}{2.576} \tag{15}$$

$$SNR = 10\log_{10}\left[\frac{\sum_{i=1}^{k}\left(I_{exa}^{i}\right)^{2}}{\sum_{i=1}^{k}\left(I_{mea}^{i} - I_{exa}^{i}\right)^{2}}\right] \tag{16}$$

The noises γ = 1%, 3% and 5% are considered and their corresponding signal-to-noise ratios (*SNR*s) of 48 dB, 38 dB and 34 dB are defined by Eq. (16). The flame is divided into $N_z \times N_r \times N_\varphi$ = 6×8×10 voxels. The reconstructed flame temperature and their relative errors under different noise levels obtained by the optimized and original samplings are shown in Figs. 6 and 7. It can be seen that the proposed optimized sampling reconstructs the flame temperature successfully even with the maximum noise. A small relative error between the original and optimized samplings was found, as shown in Fig. 7.

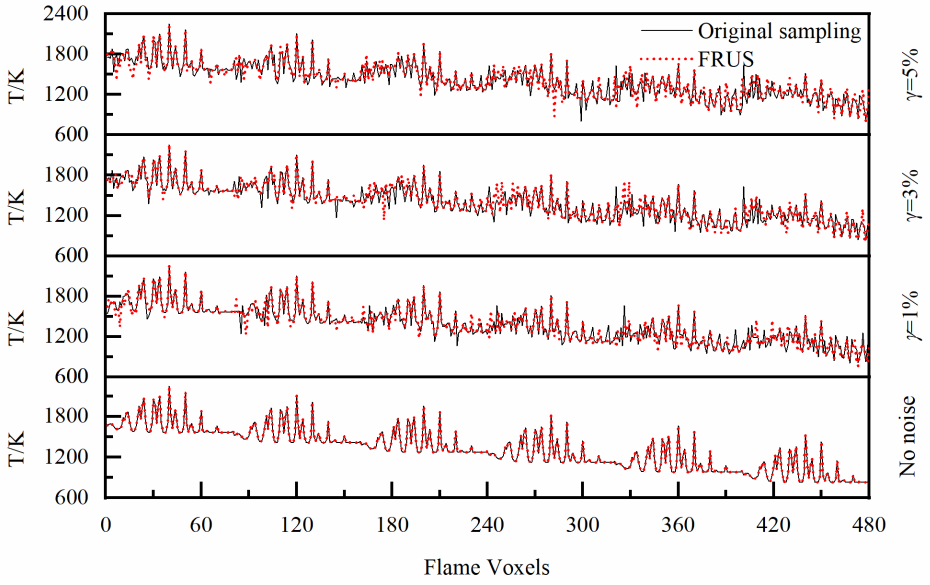

Fig. 6. The reconstructed flame temperature under different noise levels.

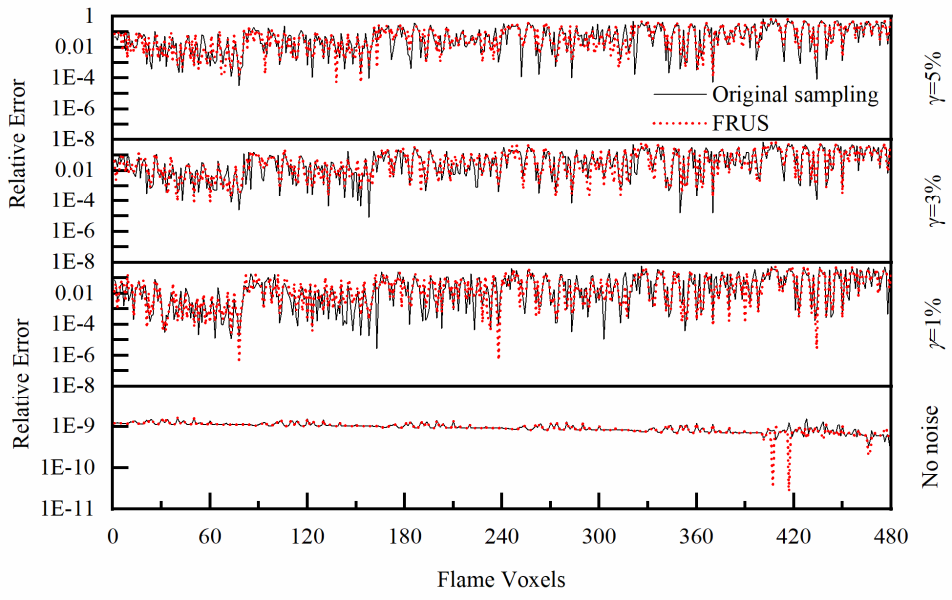

Fig. 7. The relative error of flame temperature under different noise levels.

Table 3 demonstrates the reconstruction time, mean and maximum relative errors with and without noises. The maximum and mean relative errors are increases with the increasing of noises. There is a small difference of maximum and mean relative errors between the original and optimized samplings under different noises. However, the reconstruction time is significantly reduced with the optimized sampling obtained by the FRUS approach compared to the original sampling, such as the reconstruction time with original sampling is 205.0 s, nevertheless 31s is required for the optimized samplings under γ = 1%. It is also evident that the proposed FRUS approach has excellent capability to reconstruct flame temperature with noisy flame data.

Table 3. The reconstruction time, mean and maximum relative errors under different noise levels.

Noise levels	Reconstruction Time/s		Relative Error			
	Original sampling	FRUS	Maximum		Mean	
			Original	FRUS	Original	FRUS
No noise	323.0	31.0	1.63E-09	1.63E-09	9.64E-10	9.53E-10
γ = 1%	205.0	20.0	0.595	0.541	0.067	0.067
γ = 3%	178.0	15.0	0.743	0.667	0.089	0.090
γ = 5%	150.0	14.0	0.742	0.683	0.105	0.101

3.3 Effects of flame dividing voxel

The flame dividing voxel ($N_z \times N_r \times N_\varphi$) has a significant influence on the light field sampling

thus in the reconstruction accuracy. In this study, six different cases of flame dividing voxel are considered to investigate the performance of the optimized sampling of the FRUS approach. Table 4 presents an overview of the sampling performance under different flame dividing voxels. The proposed FRUS approach optimizes the light field samplings in each case. Fig. 8 shows the results of ray tracing obtained under the six different cases. Since the camera parameters are fixed [refer to Table 2], the angular information of each ray is invariable. When the flame voxel is divided sparsely, a large number of detection rays pass through the same voxels, thus a higher redundancy of rays can be observed. When the number of flames dividing voxels is increased, the number of rays that pass through the same voxels are decreased. Therefore, the results indicate that the number of optimized rays is smaller and more redundant when the flame voxels are divided sparsely compared to the densely divided. As the number of flame dividing voxels rises, the redundancy of rays decreases and the number of optimized rays increases.

Table 4. The number of feature rays and reconstruction time.

Case	Dividing voxel	Number of feature rays		Reconstruction time/s	
		Original sampling	FRUS (optimize)	Original reconstricion	FRUS (Optimized reconstruction)
1	3×4×5	28867	2751	11.8	0.3
2	4×5×6	28867	3331	23.0	0.7
3	5×6×8	28867	4279	58.0	4.1
4	6×8×10	28867	5070	205.6	20.0
5	8×9×10	28867	6321	818.0	94.3
6	8×10×12	28867	6343	1806.0	218.0

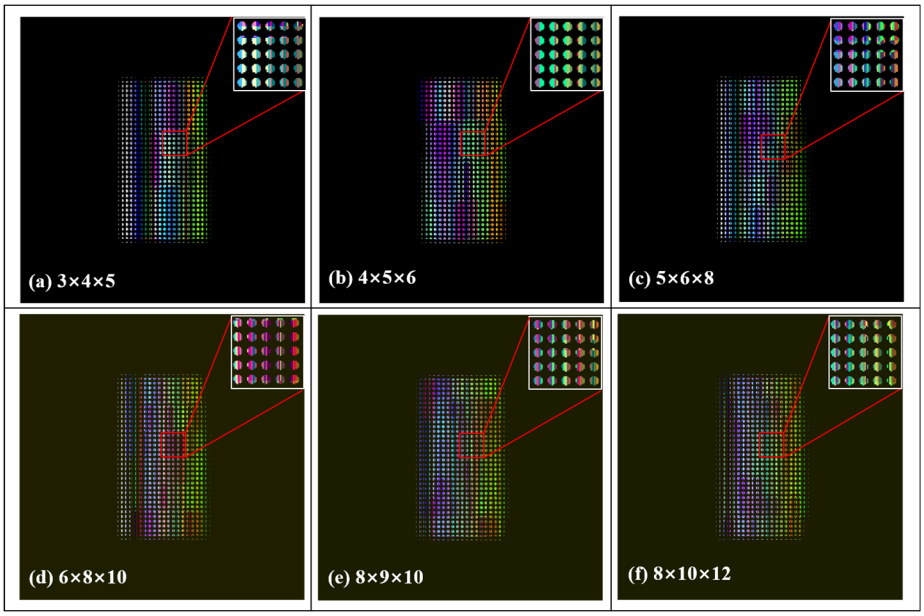

Fig. 8. Ray tracing results under different flame dividing voxels.

The reconstruction performance of the flame temperature is also investigated for both original and optimized samplings by using a bimodal flame structure [Fig. 5b]. Noise $\gamma = 1\%$ is considered. The corresponding reconstruction error and time are shown in Fig. 9 and Table 4. It can be seen that the flame temperature field is reconstructed accurately with the proposed optimized sampling, and a small difference of maximum and mean relative errors can be found between the original and optimized samplings. However, a significant difference can be seen in reconstruction time for both original and optimized samplings. For example, when the flame voxel is $N_z \times N_r \times N_\varphi = 8 \times 10 \times 12$, the reconstruction time with original sampling is 1806.0 s, whilst 218.0 s is needed for the optimized samplings. The reconstruction time is very short with sparse voxels such as 0.3 s for Case 1 and 0.7 s for Case 2. Which is expected to be used in the real-time reconstruction of flame temperature. Therefore, it is suggested that the FRUS approach can optimize the light field sampling effectively even with the different flame dividing voxels and thus improve the reconstruction time and accuracy.

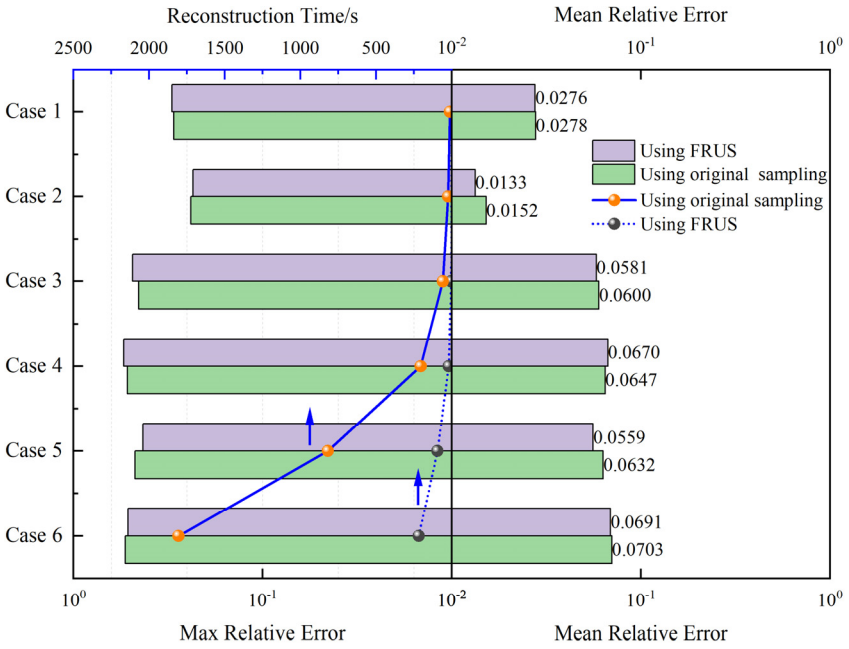

Fig. 9. Reconstruction error and time under different flame dividing voxels for original and optimized sampling.

3.4 Effects of different light field cameras

Based on the distance between the microlens array and photosensor, the light field camera can be divided into traditional ($L_{mp} = 1.0 \times f_m$) and focused light field camera ($L_{mp} \neq 1.0 \times f_m$). To investigate the sampling characteristics of the different light field cameras, numerical simulations were carried out. The input parameters used in the simulation are listed in Table 5. The sampling characteristics of different light field cameras obtained under the flame dividing voxels $N_z \times N_r \times N_\varphi = 6 \times 8 \times 10$ are shown in Fig. 10. It indicates that different light field cameras have different samplings characteristics. For the traditional light field camera, almost all rays under a microlens pass through the same flame voxels. Whereas the opposite trend can be seen for the focused light field cameras. The distribution of effective rays is also different which is more dispersed for the focused light field camera and denser for the traditional camera as shown in Fig. 10(c) and (d). The FRUS approach is used to optimize the samplings for the different light field cameras. Table 5 illustrates the number of original and optimized rays.

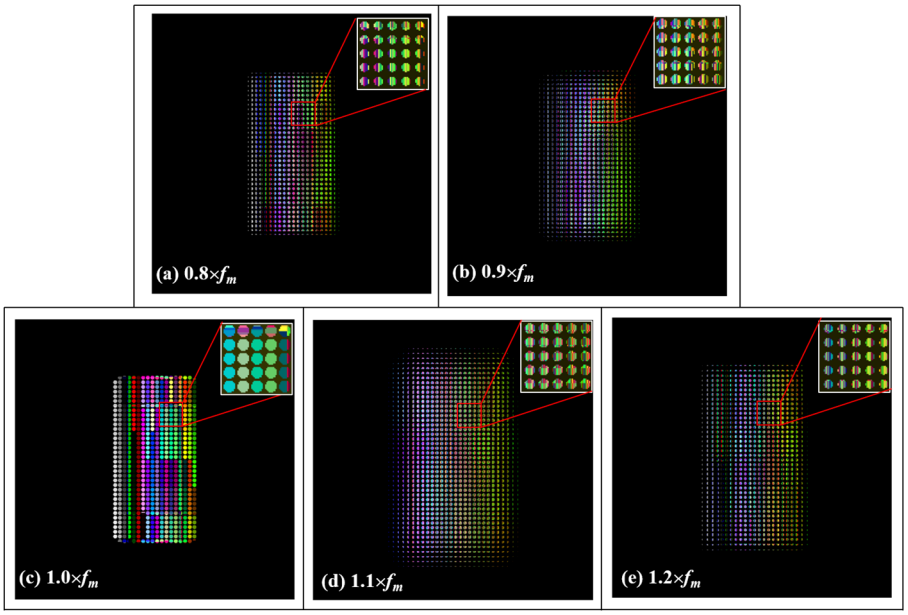

Fig. 10. The sampling characteristics of different light field cameras.

Table 5. Parameters of the light field camera.

L_{om}	L_{mm}	$L_{mp}(\times f_m)$	L_{mi}	L_{im}	f	f_m	N_m	N_p	d_p	Number of rays	
										Original sampling	FRUS (optimize)
505	53.1	0.8	55.5	-2.4	50	0.6	60	12	0.008	28867	5070
505	50.1	0.9	55.5	-5.4	50	0.6	60	12	0.008	33670	4603
505	55.5	1.0	55.5	0.0	50	0.6	60	12	0.008	52816	9085
505	62.1	1.1	55.5	6.6	50	0.6	60	12	0.008	51690	7680
505	59.1	1.2	55.5	3.6	50	0.6	60	12	0.008	35328	5823

The reconstruction performance is also verified for the different light field cameras using the original and optimized samplings with noise $\gamma = 1\%$. The bimodal flame is considered for this verification. The reconstruction results are shown in Fig. 11. It can be seen that the flame temperature can be reconstructed through optimized sampling successfully. The focused light field cameras with $L_{mp} = 0.8$, 0.9, and $1.2\times f_m$ perform better in the reconstruction. A slight difference of mean and maximum relative errors can be observed between the original and optimized samplings. The reconstruction time is shorter for the optimized sampling which is 1/10 of the original sampling. It is suggested that the FRUS approach optimizes the sampling of different light field cameras successfully and reduces the reconstruction time.

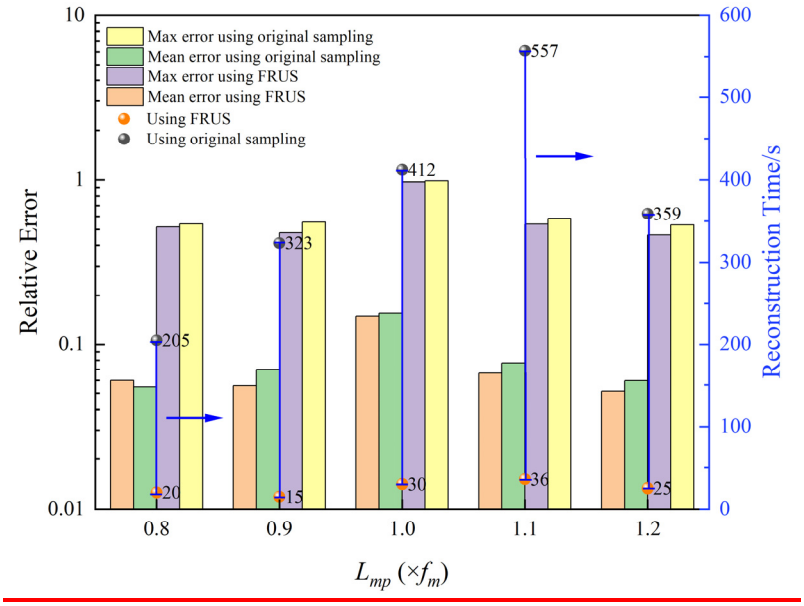

Fig. 11. Reconstruction error and time of different light field cameras.

3.5 Effects of under-sampling methods

It is crucial to investigate the reconstruction performance under different under-sampling methods. Because different under-sampling methods can result in diverse precision of flame temperature reconstruction. The random under-sampling (RUS) method is used to reconstruct the flame temperature and compared with the proposed FRUS approach. The reconstruction was carried out under the unimodal and bimodal simulated flames and the flame is divided into $N_z \times N_r \times N_\varphi = 6 \times 8 \times 10$ voxels. The parameters of the light field camera are utilized in this investigation as shown in Table 2. A total of 5070 feature rays are used for the reconstruction using the FRUS approach. To compare the reconstruction results, the RUS method is also used to select the same number of rays randomly for reconstruction. The reconstructed flame temperature distribution under different sampling methods with noise $\gamma = 1\%$ is shown in Fig. 12. It can be seen that the proposed FRUS approach reconstructs the flame temperature successfully.

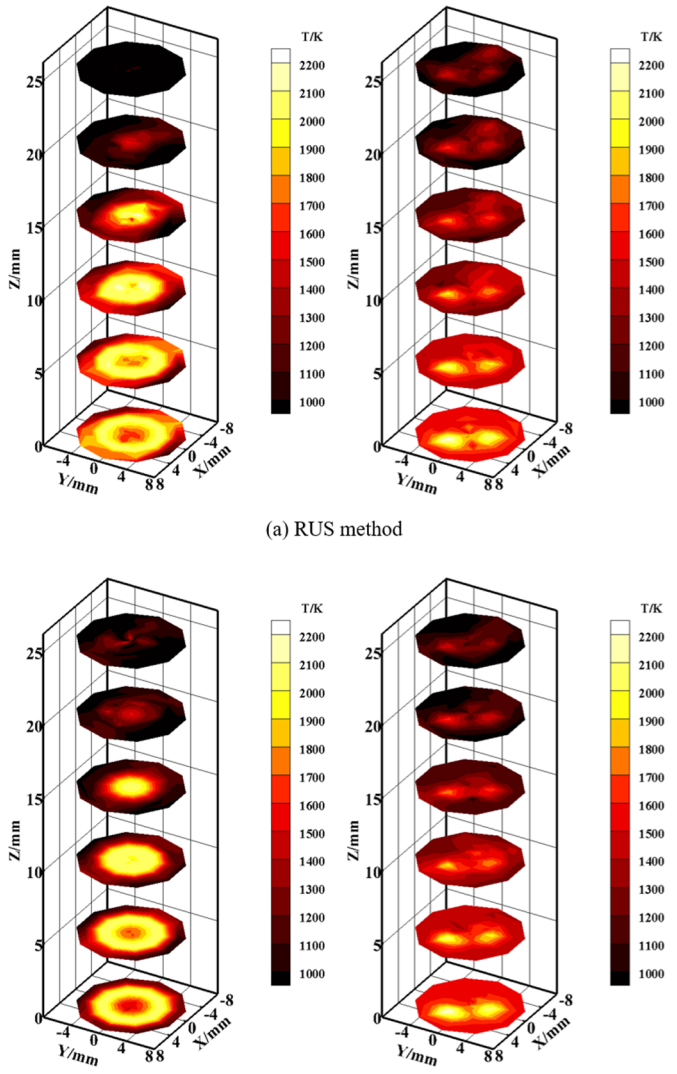

(a) RUS method

(b) FRUS approach

Fig. 12. The reconstructed temperature distributions of different simulated flames obtained under the FRUS and RUS methods.

To verify the performance of the RUS and FRUS approaches, the reconstruction without noise was repeated ten times and their maximum and mean relative errors are plotted in Fig. 13. It can be seen that the relative errors are varied significantly between the RUS and FRUS approach. An accurate and stable reconstruction performance can be seen for the FRUS samplings. Whereas a poor reconstruction quality is observed for the RUS. Therefore, it is suggested that the FRUS approach can optimize light field sampling effectively.

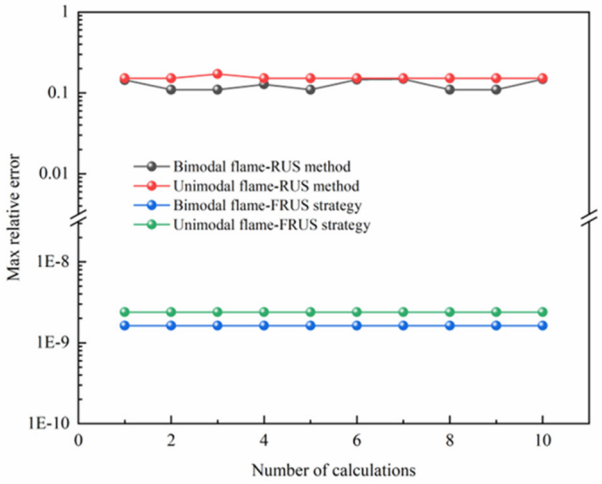

(a) Max relative error

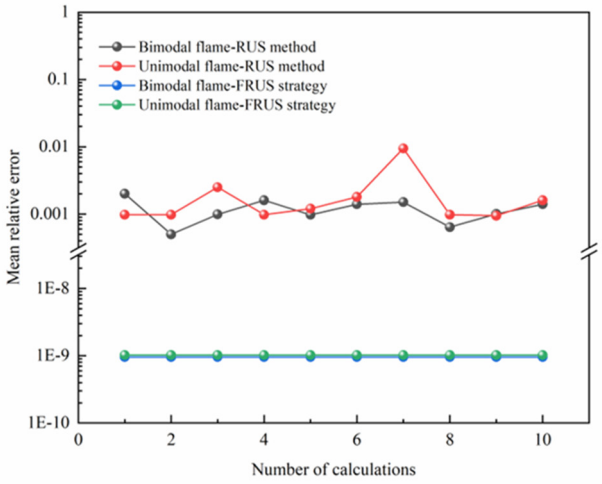

(b) Mean relative error

Fig. 13. The relative errors of reconstructed temperature under different sampling methods.

4. Experimental results and discussion

To demonstrate the performance of the proposed FRUS approach, experiments were carried out to reconstruct the temperature distributions of ethylene (C_2H_4) diffusion flames. Fig. 14 illustrates the experimental setup of the cage type light field imaging system. The setup mainly consists of a light field camera, a co-flow burner and a data acquisition system that used to collect light field flame images. The focal length of the main lens is 50 mm. The size of the microlens is 100×100 μm and $f\#$ = 4.2, respectively. The light field camera sensor has a resolution of 3312 (H)×2488 (V) with a pixel size of 5.5 μm. The detailed structure of the light field camera can be found in Ref. [19]. The camera is placed on a supporting plate that can be

lifted and rotated. The exposure time of the camera is set to 170 μs to ensure the captured flame images are not too dark and not saturated. The light field flame images are captured under three combustion operation conditions (i.e., air to fuel equivalence ratio, λ), they are shown in Table 6. The λ is defined as the ratio of the actual air/fuel ratio to the stoichiometric air/fuel ratio [28]. Fig. 15 shows the captured flame images under three different equivalence ratios. It can be seen that the flame height becomes larger when the fuel flow rates are increased.

Table 6. Combustion operation conditions.

λ	Fuel (L/min)	Air (L/min)
23.39	0.08	
8.64	0.10	3.00
5.76	0.12	

The captured flame is divided into $N_z \times N_r \times N_\varphi$ = 10×10×15 voxels. The proposed FRUS approach is employed to obtain optimized light field samplings. The reconstructed temperature distributions under original sampling, RUS sampling and FRUS sampling are shown in Fig. 16. It can be seen that the reconstructed flame temperature varies from 800 K to 2100 K, which is agreed with the results obtained by Santoro *et al*. [39]. For each condition, it can be seen that the flame temperature increases and then decreases from the inner to the edge of the flame. The temperature also increases with the ethylene flow rate due to the greater heat release during the combustion reaction. Comparing Fig. 16 (a) with (b) and (c), it can be seen that there is a small difference between the original and FRUS optimized samplings under different equivalent ratios. However, the differences between original and RUS samplings are quite obvious. Meanwhile, the reconstruction times for each condition are recorded as 209 s, 285 s and 327 s with FRUS sampling, respectively. Therefore, it is evident that the FRUS approach is effective for optimizing light field sampling, which does not only reduce the sampling's redundancy but also improves the reconstruction efficiency.

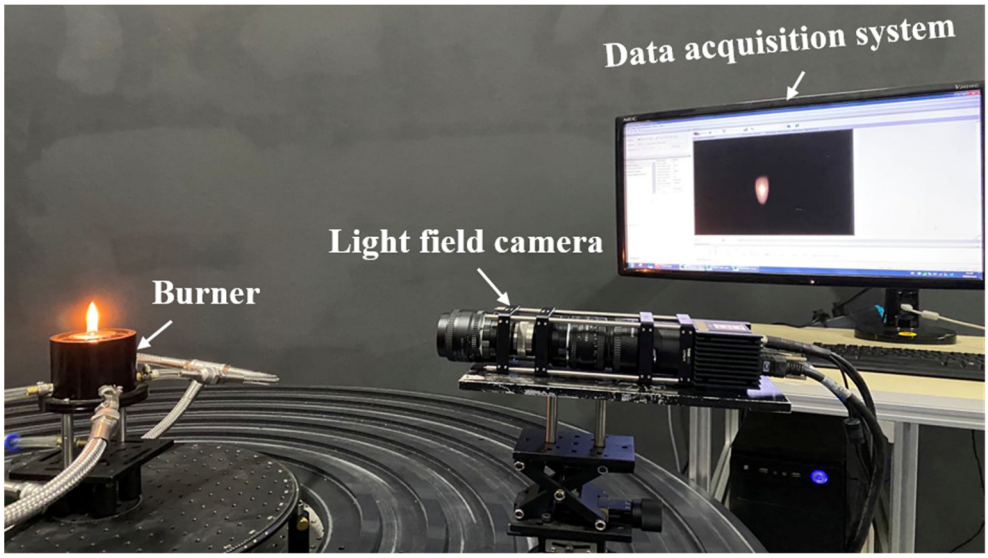

Fig. 14. Experimental setup of the cage type light field imaging system.

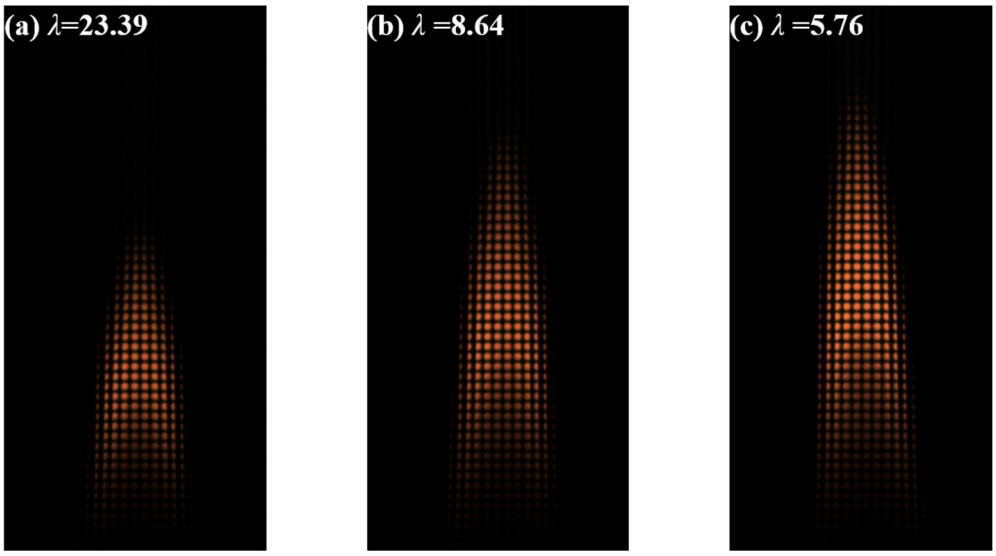

Fig. 15. Example of light filed flame images captured under different equivalent ratios.

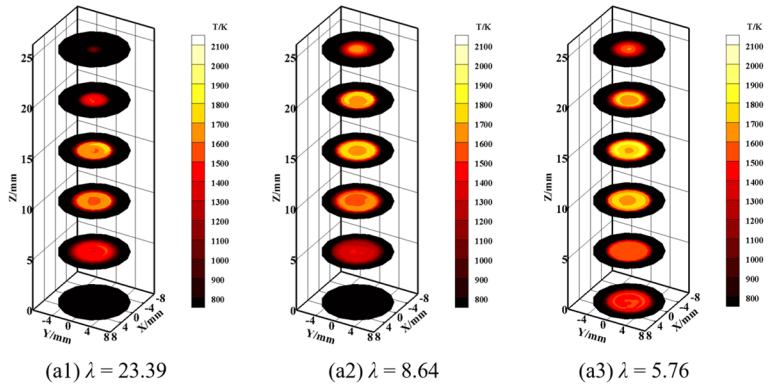

(a1) λ = 23.39 (a2) λ = 8.64 (a3) λ = 5.76

(a) Original sampling

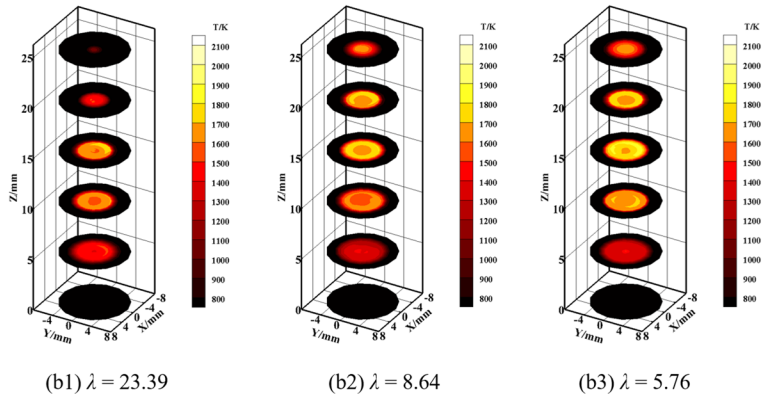

(b1) λ = 23.39 (b2) λ = 8.64 (b3) λ = 5.76

(b) FRUS approach

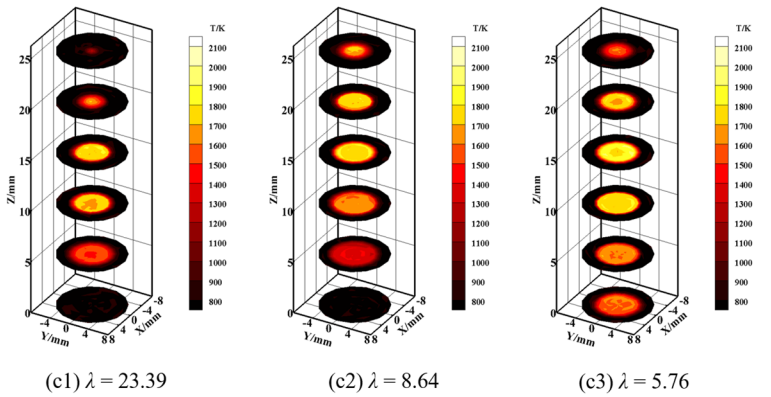

(c1) λ = 23.39 (c2) λ = 8.64 (c3) λ = 5.76

(c) RUS method

Fig. 16. The reconstructed temperature distributions over cross-section of ethylene diffusion flames under different equivalent ratios.

5. Conclusions

A novel feature rays under-sampling approach is proposed to reduce the light field sampling's

redundancy and improve the reconstruction efficiency. Effects of light field under-sampling methods, noise levels, flame dividing voxels and light field camera parameters are investigated. Experiments were conducted to verify the efficiency and applicability of the proposed approach. The concluding remarks obtained from this study are summarized as follows.

- The proposed approach has excellent performance under different noise levels and light field camera parameters, a small difference of maximum and mean relative errors were found between the original and optimized samplings.
- It has been observed that the number of optimized rays is smaller and more redundant when the flame voxels are divided sparsely compared to the densely divided. An accurate and stable reconstruction performance is found for the FRUS sampling compared to the RUS.
- The reconstruction time is significantly reduced by the FRUS approach compared to the original sampling. It is suggested that the FRUS approach can optimize light field sampling effectively.

Further work will focus on the optimization of a light field imaging system based on the proposed approach.

Funding. National Natural Science Foundation of China (51976038); National Natural Science Foundation of Jiangsu Province (BK20201279).

Acknowledgments. This work was supported by the National Natural Science Foundation of China [grant number 51976038]; the National Natural Science Foundation of Jiangsu Province [grant number BK20201279]; and the Scientific Research Foundation of Graduate School of Southeast University.

Disclosures. The authors declare no conflicts of interest.

References

1. M. Rilling, L. Archambault, and S. Thibault, "Simulating imaging-based tomographic systems using optical design software for resolving 3D structures of translucent media," Appl. Opt. **58**, 5942-5951 (2019).
2. Q. N. Chan, P. R. Medwell, P. A. M. Kalt, Z. T. Alwahabi, B. B. Dally, and G. J. Nathan, "Simultaneous imaging of temperature and soot volume fraction," Proc. Combust. Inst. **33**, 791-798 (2011).
3. M. J. He, H. Qi, Y. F. Wang, Y. T. Ren, W. H. Cai, and L. M. Ruan, "Near-field radiative heat transfer in multilayered graphene system considering equilibrium temperature distribution," Opt. Express **27**, A953-A966 (2019).
4. J. Salinero, A. Gómez-Barea, D. Fuentes-Cano, and B. Leckner, "The effect of using thermocouples on the char particle combustion in a fluidized bed reactor," Fuel **207**, 615-624 (2017).
5. P. Sun, Z. Zhang, Z. Li, Q. Guo, and F. Dong, "A Study of Two Dimensional Tomography Reconstruction of Temperature and Gas Concentration in a Combustion Field Using TDLAS," Applied Sciences **7**, 990 (2017).
6. C. M. Mitsingas, S. D. Hammack, E. K. Mayhew, R. Rajasegar, B. McGann, A. W. Skiba, C. D. Carter, and T. Lee, "Simultaneous high speed PIV and CH PLIF using R-branch excitation in the C2Σ+-X2Π (0,0) band," Proc. Combust. Inst. **37**, 1479-1487 (2019).

7. M. Hofmann, W. G. Bessler, C. Schulz, and H. Jander, "Laser-induced incandescence for soot diagnostics at high pressures," Appl. Opt. **42**, 2052-2062 (2003).
8. K. Wang, F. Li, H. Zeng, and X. Yu, "Three-dimensional flame measurements with large field angle," Opt. Express **25**, 21008-21018 (2017).
9. M. M. Hossain, G. Lu, and Y. Yan, "Optical Fiber Imaging Based Tomographic Reconstruction of Burner Flames," IEEE Transactions on Instrumentation & Measurement **61**, 1417-1425 (2012).
10. S. S. Aphale and P. E. DesJardin, "Development of a non-intrusive radiative heat flux measurement for upward flame spread using DSLR camera based two-color pyrometry," Combust. Flame **210**, 262-278 (2019).
11. M.-J. He, H. Qi, Y.-T. Ren, Y.-J. Zhao, and M. Antezza, "Graphene-based thermal repeater," Appl. Phys. Lett. **115**(2019).
12. Z. P. Tan, K. Johnson, C. Clifford, and B. S. Thurow, "Development of a modular, high-speed plenoptic-camera for 3D flow-measurement," Opt. Express **27**, 13400-13415 (2019).
13. J. Floyd, P. Geipel, and A. M. Kempf, "Computed Tomography of Chemiluminescence (CTC): Instantaneous 3D measurements and Phantom studies of a turbulent opposed jet flame," Combust. Flame **158**, 376-391 (2011).
14. M. M. Hossain, G. Lu, D. Sun, and Y. Yan, "Three-dimensional reconstruction of flame temperature and emissivity distribution using optical tomographic and two-colour pyrometric techniques," Meas. Sci. Technol. **24**, 074010 (2013).
15. E. H. Adelson and J. Y. A. Wang, "Single Lens Stereo with a Plenoptic Camera," IEEE Trans. Pattern Anal. Mach. Intell. **14**, 99-106 (1992).
16. J. Sun, C. Xu, B. Zhang, M. M. Hossain, S. Wang, H. Qi, and H. Tan, "Three-dimensional temperature field measurement of flame using a single light field camera," Opt. Express **24**, 1118-1132 (2016).
17. D. Kelly, "Development of a Multi-band Plenoptic Camera for High Temperature Measurements," (Auburn University, Auburn, Alabama, 2020).
18. Zhao W , Zhang B , and X. C, "Optical Sectioning Tomographic Reconstruction of Three-dimensional Flame Temperature Distribution Using Single Light Field Camera," IEEE Sensors Journal **18**, 528-539 (2018).
19. Q. Qi, M. M. Hossain, B. Zhang, T. Ling, and C. Xu, "Flame temperature reconstruction through a multi-plenoptic camera technique," Meas. Sci. Technol. **30**, 124002 (2019).
20. H. Liu, Q. Wang, and W. Cai, "Assessment of plenoptic imaging for reconstruction of 3D discrete and continuous luminous fields," Journal of the Optical Society of America A **36**, 149-158 (2019).
21. X. Huang, H. Qi, C. Niu, L. Ruan, H. Tan, J. Sun, and C. Xu, "Simultaneous reconstruction of 3D temperature distribution and radiative properties of participating media based on the multi-spectral light-field imaging technique," Appl. Therm. Eng. **115**, 1337-1347 (2017).
22. L.-Y. Wei, C.-K. Liang, G. Myhre, C. Pitts, and K. Akeley, "Improving light field camera sample design with irregularity and aberration," ACM Trans. Graph. **34**, Article 152 (2015).
23. D. C. Schedl, C. Birklbauer, and O. Bimber, "Optimized sampling for view interpolation in light fields using local dictionaries," Comput. Vision Image Understanding **168**, 93-103 (2018).
24. M.-K. Park, H. Park, K.-I. Joo, T.-H. Lee, K.-C. Kwon, M.-U. Erdenebat, Y.-T. Lim, N. Kim, and H.-R. Kim, "Fast-switching laterally virtual-moving microlens array for enhancing spatial resolution in light-field imaging

system without degradation of angular sampling resolution," Sci. Rep. **9**, 11297 (2019).

25. H. Huang and H. Hua, "Effects of ray position sampling on the visual responses of 3D light field displays," Opt. Express **27**, 9343-9360 (2019).
26. C. Zhu, H. Zhang, Q. Liu, Y. Yu, and H. Su, "Frequency analysis of light field sampling for texture information," Opt. Express **28**, 11548-11572 (2020).
27. Y. Liu, M. M. Hossain, J. Sun, B. Zhang, and C. Xu, "Investigation and optimization of sampling characteristics of light field camera for flame temperature measurement," Chin. Phys. B **28**, 034207 (2019).
28. J. Sun, M. M. Hossain, C. Xu, and B. Zhang, "Investigation of flame radiation sampling and temperature measurement through light field camera," Int. J. Heat Mass Transfer **121**, 1281-1296 (2018).
29. M. Levoy, Z. Zhang, and I. Mcdowall, "Recording and controlling the 4D light field in a microscope using microlens arrays," J. Microsc. **235**, 144-162 (2010).
30. A. Gershun, "The Light Field," J. Math. Phys. **18**, 51-151 (1939).
31. C.-Y. Niu, H. Qi, X. Huang, L.-M. Ruan, W. Wang, and H.-P. Tan, "Simultaneous reconstruction of temperature distribution and radiative properties in participating media using a hybrid LSQR–PSO algorithm," Chin. Phys. B **24**, 114401 (2015).
32. C.-Y. Niu, H. Qi, X. Huang, L.-M. Ruan, and H.-P. Tan, "Efficient and robust method for simultaneous reconstruction of the temperature distribution and radiative properties in absorbing, emitting, and scattering media," J. Quant. Spectrosc. Radiat. Transfer **184**, 44-57 (2016).
33. L. Zhao and G. Shi, "A method for simplifying ship trajectory based on improved Douglas–Peucker algorithm," Ocean Eng. **166**, 37-46 (2018).
34. J. Li, M. M. Hossain, J. Sun, Y. Liu, B. Zhang, C. Tachtatzis, and C. Xu, "Simultaneous measurement of flame temperature and absorption coefficient through LMBC-NNLS and plenoptic imaging techniques," Appl. Therm. Eng. **154**, 711-725 (2019).
35. J. D. Felske and C. L. Tien, "Calculation of the Emissivity of Luminous Flames," Combustion Science & Technology **7**, 25-31 (1973).
36. G. Legros, Q. Wang, J. Bonnety, M. Kashif, C. Morin, J.-L. Consalvi, and F. Liu, "Simultaneous soot temperature and volume fraction measurements in axis-symmetric flames by a two-dimensional modulated absorption/emission technique," Combust. Flame **162**, 2705-2719 (2015).
37. C. L. Lawson and R. J. Hanson, *Solving Least Squares Problems*, Section 3. PROBLEM NNLS (Society for Industrial and Applied Mathematics, Philadelphia, 1995), Vol. 15, pp. 160-165.
38. R. J. Santoro, T. T. Yeh, J. J. Horvath, and H. G. Semerjian, "The Transport and Growth of Soot Particles in Laminar Diffusion Flames," Combust. Sci. Technol. **53**, 89-115 (1987).
39. R. J. Santoro, H. G. Semerjian, and R. A. Dobbins, "Soot particle measurements in diffusion flames," Combust. Flame **51**, 203-218 (1983).